Interaction between systems and materials in fretting

A. Benítez, J. Denape, J.-Y. Paris *

[a] Laboratoire Génie de Production (LGP), Université de Toulouse, INP-ENIT, 65016 Tarbes Cedex, France

Keywords:
Fretting wear
Electrical contacts
Control system mode
Non-ferrous metals
Acoustic emission

A B S T R A C T

Most fretting studies analyze material's responses using criteria directly issued from characteristic parameters of the fretting loops (loop aperture, dissipated energy, contact stiffness…). The present study concerns the influence of the device, first element of the tribological triplet, on the gross slip response of a ball on flat contact. The role of the static and dynamic device stiffness (vibratory analysis), of the control system mode (imposed displacement or imposed actuator force) and of the material type (ductile or brittle) on the loop shape is analyzed in order to distinguish the respective contributions of devices and materials.

1. Introduction

Fretting affects most of the mechanical assemblies (quasi static joining) when cyclic movements of low displacement amplitude occur because of environmental vibrations or thermal stresses. This mechanical loading is one of the main causes affecting the durability of electrical connectors in the area of transportation. The fretting is therefore a serious problem in terms of reliability in embedded electronic systems due to disruptions in signal trans missions as the consequence of an irreversible loss of electrical conductivity in the contacting materials [1 3].

Depending on the stress conditions (applied load, displacement amplitude) and the pairs of contact materials, the damage can take the form of debris formation (fretting wear) or crack propagation (fretting fatigue) [4]. The boundary between the sliding regimes by fretting fatigue and fretting wear is identified using criteria directly derived from the characteristic parameters of fretting loops (loop aperture, dissipated energy). The accurate analysis of fretting loops plays therefore a central role to understanding the behavior of materials under such conditions.

An ideal fretting loop under total slip regime controlled in position should have a symmetrical quadratic form (Fig. 1a) lead ing to a constant tangential friction force during the sliding phase (horizontal lines) and an overall infinite stiffness (vertical lines) in the sliding direction changes. In fact, the literature shows various shapes of fretting loops from near rectangles to potato shaped via spindles, with hooks and looping shapes at the ends far away from the ideal case (Fig. 1b). This wide variety of shapes is attributed to different origins:

- The slope in the sliding direction changes is clearly linked to a tangential stiffness K ($K=\Delta F_T/\Delta\delta$) including the stiffness of the contact, but also that of the device [5,6].
- The hooks correspond to the arrival of the slider to the end of each fretting loop. This phenomenon can be seen in ductile materials and attributed to interactions with frontal plastic accumulations (spinning material) in the periphery of the con tact area [7,8].
- The evolution of the tangential friction force F_T during slip phases is sometimes interpreted as the result of interactions between asperities within the contact zone [9,10].

The main purpose of the present study is to show how the system stiffness and the motion control mode can influence the tribological and electrical behavior of conductive materials sub jected to fretting wear.

2. Experimental and materials

An existing experimental device had to be adapted in terms of motion control (for getting a driving control by imposed dis placement or by imposed actuator force) and electrical insulation of the contact (to measure the contact resistance). The dynamic device changes have clearly highlighted the strong interaction between device and contact material responses.

The fretting device is composed of an electrodynamic shaker LDS V406/8™ which generates reciprocating movements transmitted

* Corresponding author. Tel.: +33 5 62 44 27 25.
E-mail address: jean-yves.paris@enit.fr (J.-Y. Paris).

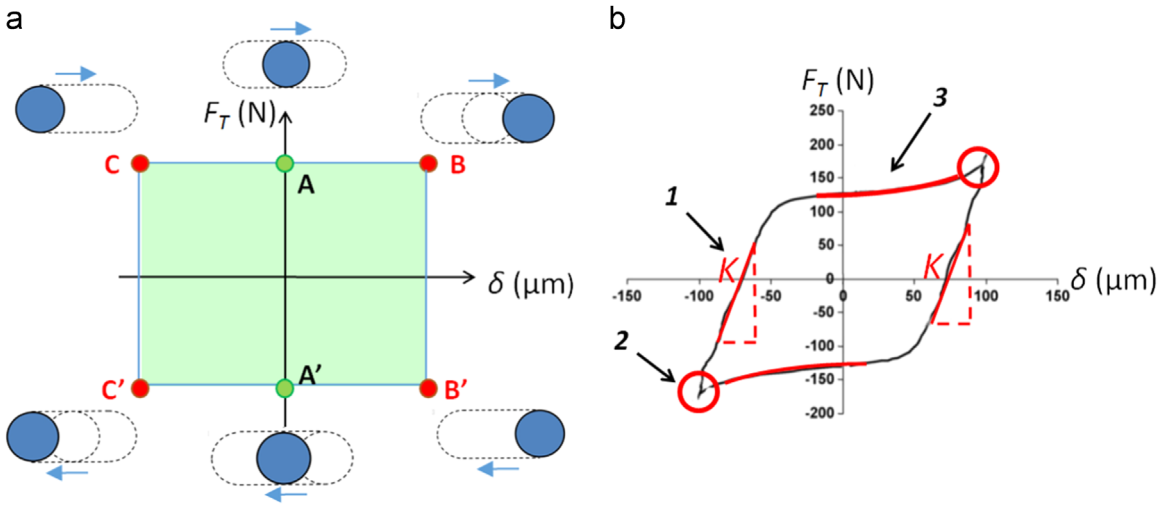

Fig. 1. (a) Ideal fretting loop in gross slip; (b) characteristics of real fretting cycle.

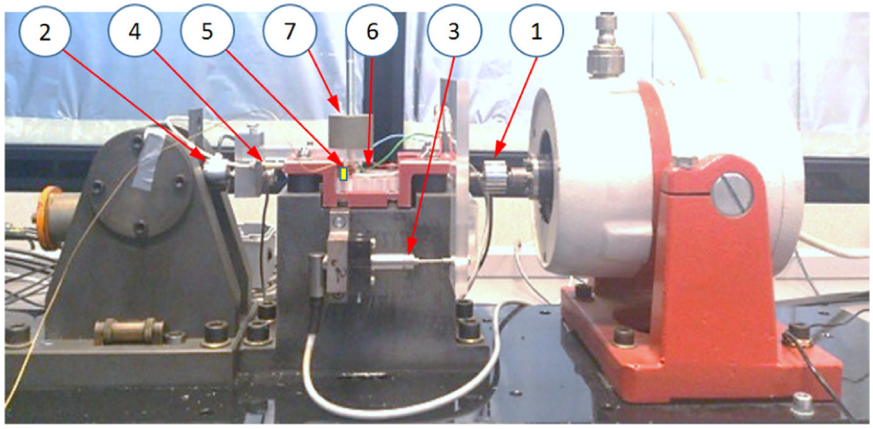

Fig. 2. Fretting device instrumentation: (1) actuator force delivered by the vibrating pot, (2) friction force, (3) displacement (frame), (4) displacement (arm), (5) acoustic emission, (6) contact resistance, (7) normal force.

towards a movable platform mounted on four elastic buffers fixed to the frame. A pivoting arm allows the normal loading by dead weight in drip line of the contact (Fig. 2). The contact configuration is sphere on flat.

The instrumentation includes:

- two force transducers (located at the outlet of the pot and on the pivoting arm, in the contact plane of the sample), measuring respectively the actuator force F_a and the tangential force F_T,
- two displacement sensors (one LVDT on the frame and one Foucault current on the arm) for controlling and measuring of the contact displacement δ,
- a four wire circuit to measure the electrical contact resistance R_c,
- an acoustic emission piezoelectric sensor to analysis default propagation inside the contact zone.

The studied material is a bronze of 6% tin weight (CuSn6), commonly used in connections due to good conductivity (7.5 S m mm ^{2} that is 13% IACS with respect to copper), good mechanical properties (micro hardness measured of 260 ± 13 HV) and cold deformation features (yield strength greater than 500 MPa, Young's modulus of 130 GPa and elongation of more than 5%).

The samples were made from a foil of 0.4 mm thick with a roughness measured of 206 ± 13.5 nm. The sample plan is a cut square of 20 mm sides. The slider was obtained by bending a rectangular foil of 40 mm by 10 mm, with a hemispherical cap of 1.5 mm radius per formed later by press forming (Fig. 3). Vickers indentation measurements on a polished cross section of the spherical part show a slight increase in micro hardness (285 ± 17 HV). All samples were cleaned by the following procedure: degreasing for 15 min using an industrial detergent Micro 90, diluted at 1%, rinsing with demineralized water, then ultrasonic cleaning for 10 min with ethanol and drying in an oven at 60 °C for 15 min. The temperature and relative humidity were 21 ± 2 °C and 60 ± 20 RH for the whole campaign of test.

3. Influence of the device compliance

Measuring the electrical contact resistance involves the electrical insulation of samples. Two configurations were studied for the arm linked to the slider (Fig. 4):

- a fully PMMA arm with a moment of inertia of $1.06 \cdot 10^{-6}$ kg m^2,
- a bi material arm formed by two parts of aluminum alloy and PMMA with a larger moment of inertia of $1.61 \cdot 10^{-3}$ kg m^2.

Tests were conducted using these two different arms with homogeneous CuSn6 CuSn6 pairs at imposed displacement amplitude $\delta_i = \pm 40$ μm for a normal load of 6 N and an excitation frequency of 10 Hz.

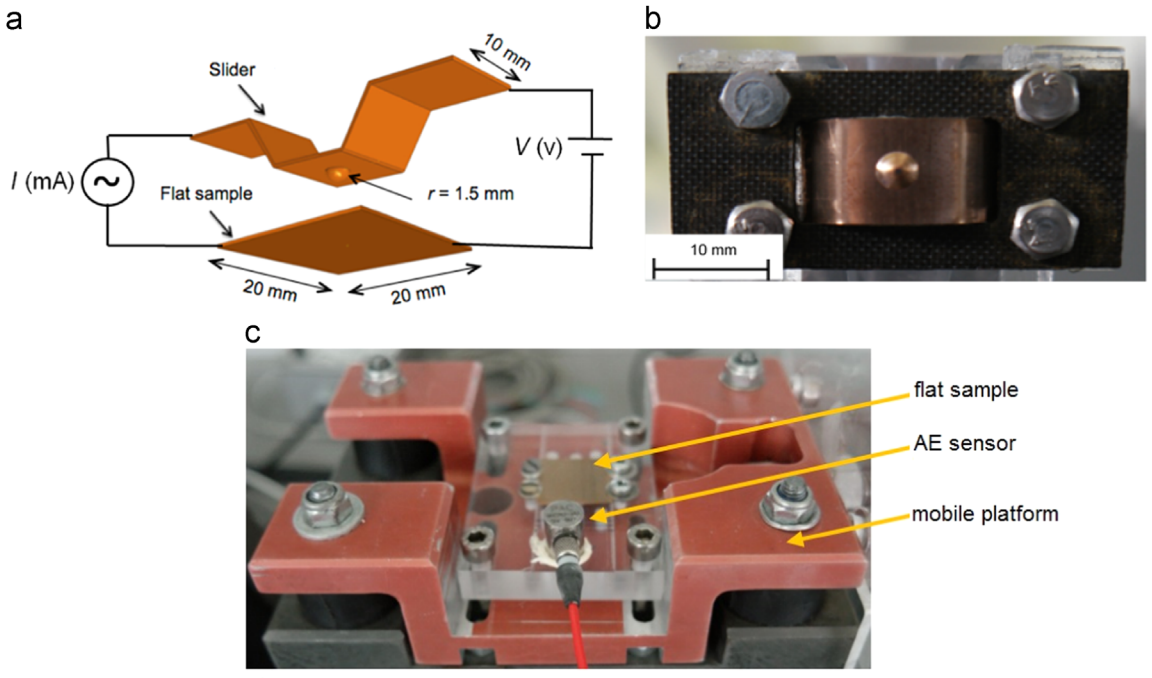

Fig. 3. (a) Shape and geometry of the fretting samples, (b) view of the slider fixed on the pivoting arm, (c) mobile platform showing the sample and AE sensor positions.

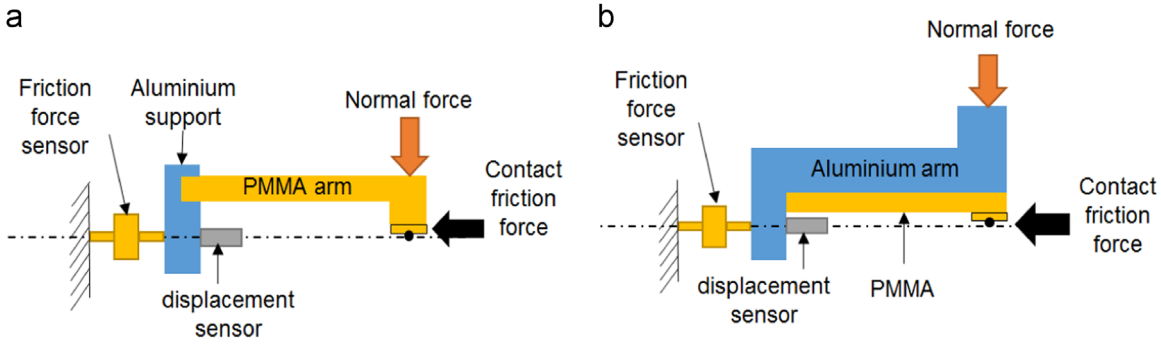

Fig. 4. Electrically isolated pivoting arms: (a) made of fully PMMA; (b) made of bi-material Al-PMMA.

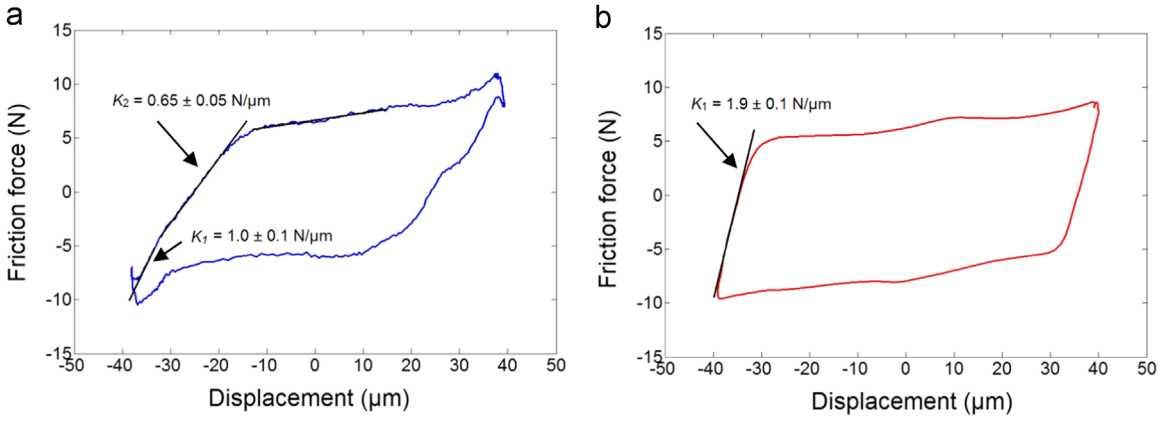

Fig. 5. Fretting loops comparison: (a) PMMA arm and (b) Al-PMMA arm (stiffer) with optimized sample holder (δ_i ±40 µm, F_N 6 N, f 10 Hz).

The fretting loops associated to the PMMA arm (most compliant) operate according to gross slip condition and present an approximate tilted quadratic shape with two hooks at the beginning of every sliding direction change (Fig. 5a). More precisely, each half loop exhibits two slopes when the direction change occurs, which could be interpreted as two different stiffnesses: the first one ($K_1 = 1.0 \pm 0.1$ N/µm) is related to the arm and contact stiffnesses, the second one ($K_2 = 0.65 \pm 0.05$ N/µm) is imputed to a slight torsional moment of the slider foil. In such conditions, the dissipated energy E_d in the contact reaches 671 ± 54 µJ/cycle.

The fretting loops associated to the Al PMMA arm (stiffest) with a reinforced sample holder using a frame of carbon fiber to avoid torsion of the upper sample (Fig. 3b), and the introduction of an alumina sphere (3 mm in diameter) stuck up between the

slider and the arm to reduce potential deformations of the slider, show a quadratic and symmetric shape, typical of a gross slip condition (Fig. 5b). The only slope associated to the change in direction ($K=1.9\pm0.1$ N/μm) is higher than in the previous case and the contact is much more dissipative ($E_d=982\pm26$ μJ/cycle).

From here, all the following results were performed using the bi material arm of higher stiffness. The global compliance C (inverse of the measured stiffness K) gathers all the possible accommodations of the system. It is the sum of the device com pliance C_d (arm, slider) and the contact compliance C_c.

The contact compliance was first evaluated on a CuSn6 CuSn6 pair at imposed actuator force $F_{ai}=\pm0.2$ N under a normal force of 6 N generating partial sliding conditions (closed loops) that is in quasi static conditions (displacements lower than 1 μm). Experimental measurements show a global compliance C of 0.40 ± 0.03 μm/N. Observations using a high speed camera Photon Focus A1312™ con firm that no relative displacement occurs on the loading arm and a finite element analysis of the slider for a tangential friction force from 1 N to 6 N gives a constant compliance of 0.10 ± 0.01 μm/N. The contact compliance C_c can be estimated to 0.30 ± 0.03 μm/N or approximately a contact stiffness K_c of 3.3 ± 0.3 N/μm in the studied conditions.

In sliding conditions (open loops), under the same normal load of 6 N but at imposed displacement of ±40 μm, the measured stiffness is now of 1.9 ± 0.1 N/μm ($C=0.53\pm0.03$ μm/N) indicating a contact compliance $C_c=0.43\pm0.04$ μm/N (or $K_c=2.33\pm0.23$ N/μm). This contact compliance is independent of the excitation frequency in the range from 5 Hz to 30 Hz (Fig. 6).

Another type of artifact, related to the measurement instru mentation can lead to misinterpretations. Thus, truncated infor mation coming from a displacement sensor (LVDT) can generate a fretting loop with a double slope during the change of sliding direction phase (Fig. 7). The vertical part in the loop is here attributed to the signal saturation and not on a physical change of the stiffness. The solution imposed the replacement of the sensor LVDT by a new one (Foucault current).

Finally, a vibratory analysis (ranging from 0 to 1 kHz) was conducted by Laser Doppler Velocimetry (LDV) using a device OMETRON VH300+™ coupled to a high speed camera. The tests were carried out with homogeneous CuSn6 CuSn6 pairs, for two imposed displacements (±15 μm and ±40 μm), at two constant normal loads (1 N and 3 N) and two excitation frequencies (10 Hz and 25 Hz). The vibration spectra recorded on the arm (quasi static part) show that the resonance frequencies slightly depend on the excitation frequency while the displacement amplitude and normal load only affect the signal intensity (Fig. 8).

4. Influence of servo-control mode

A control system from VibPilot™ was implemented on the vibrating pot to drive the movements of the mobile platform according to two possible modes: imposed displacement δ_i, or imposed actuator force F_{ai}, knowing that frequency f and normal load F_N are constant for each test. Results were performed using the bi material arm of higher stiffness.

4.1. No load conditions

The two control modes were compared without normal loading ($F_N=0$), with a constant frequency of 10 Hz for imposed forces F_{ai} ranged from 4 N to 30 N and for imposed displacements δ_i ranged from ±10 μm to ±70 μm. The results show the equivalence of these two modes in terms of measured responses, so without loading the

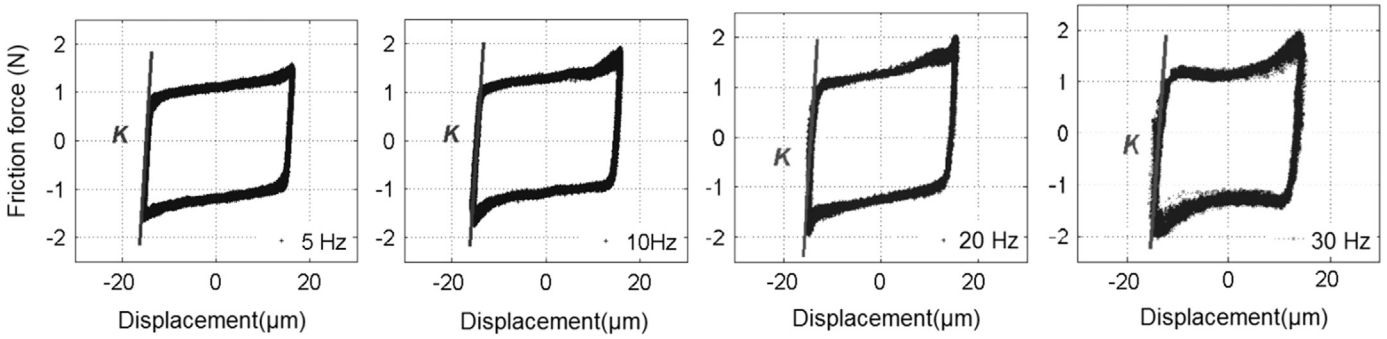

Fig. 6. Measured contact stiffness on the fretting loops at four excitation frequencies from 5 Hz to 30 Hz (δ_i ±15 μm, F_N 1 N, N_c 350 cycles).

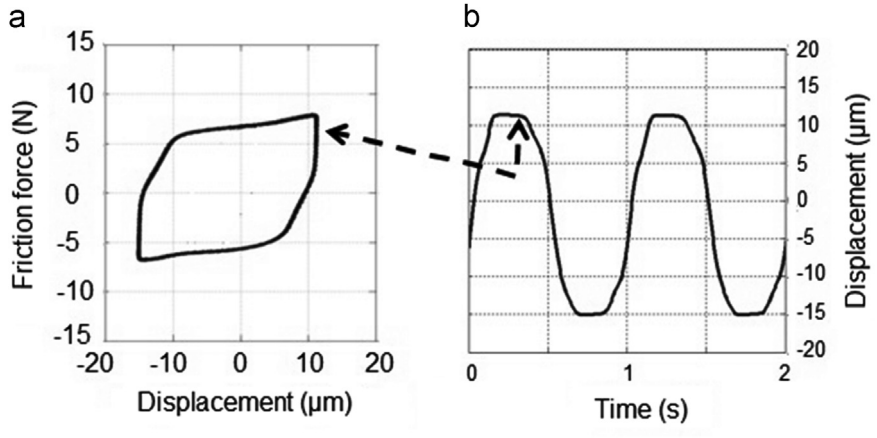

Fig. 7. (a) Fretting loop anomaly caused by a displacement sensor (b) associated to a truncated sinus.

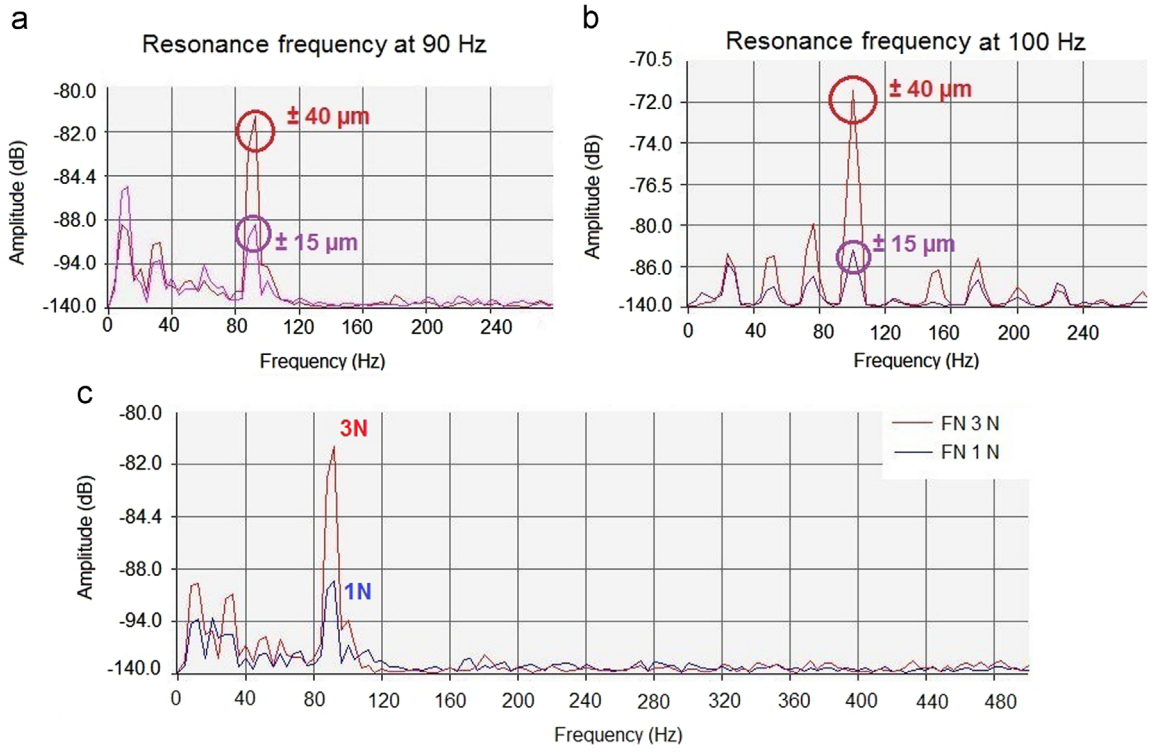

Fig. 8. Vibratory spectra registerd for CuSn6/CuSn6 contacts (a) excitation frequency of 10 Hz (F_N 3 N, δ_i ± 15 µm and ± 40 µm), (b) excitation frequency of 25 Hz (F_N 3 N, δ_i ± 15 µm and ± 40 µm), (c) excitation frequency of 10 Hz (F_N 1_N and 3 N, δ_i ± 40 µm).

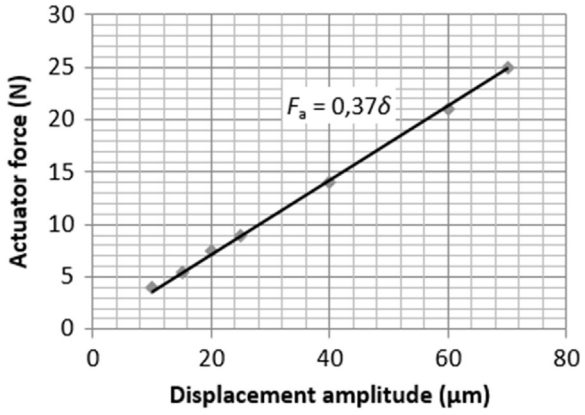

Fig. 9. Equivalence between imposed displacement and imposed actuator force without normal loading.

amplitude displacement of movable platform is proportional to imposed actuator force, that confirm the linear deformation of elastic buffers on all displacement amplitude device (Fig. 9).

4.2. Incremental loading conditions

Tests were carried out with homogeneous CuSn6 CuSn6 pairs with load increments from 1 N to 8 N by steps of 1 N every 200 cycles. At imposed displacement ($\delta_i = \pm 15$ µm), the displacement amplitude (set) must be maintained, so the control system increases the actuator force F_{ai} to overcome the tangential force F_T that regularly increases with load increments (Fig. 10a). The contact works only in gross sliding regime because the imposed force F_{ai} is always greater than the friction force F_T. The coefficient of friction, defined as the ratio of the mean friction force for each cycle on the corresponding normal load, remains stable throughout the test, whereas the dissipated energy E_d (calculated by integrating the fretting loop along the displacement axis and the tangential force axis that corresponds to the loop area) increases in accordance with the normal load rise (Fig. 10b).

At imposed actuator force ($F_{ai} = \pm 6$ N), the contact adapts by increasing the tangential force and reducing the displacement amplitude according to the contact response (Fig. 11a). The contact progressively shifts from a gross sliding mode towards a sticking mode. This sticking mode occurs when the value of the tangential force reaches that of the actuator force (set) that means $F_T = F_a$. In these test conditions, dissipated energy only varies very little and the friction coefficient (during gross sliding mode) or more exactly the ratio F_T/F_N (during partial slip and sticking modes) decreases with the normal load (Fig. 11b).

4.3. Constant loading conditions

Next, tests were conducted under constant operating conditions. As discussed above, under a given normal load, an imposed displacement δ_i requires a certain actuator tangential force F_a to involve such contact displacement. Inversely, an imposed actuator force F_{ai} implies certain displacement amplitude. In this way, under a constant load $F_N = 1$ N, an imposed actuator force $F_{ai} = \pm 15$ N leads to a relative displacement $\delta = \pm 40$ µm.

Two tests were carried out with homogeneous CuSn6/CuSn6 pairs in dry conditions, at an excitation frequency $f = 10$ Hz and a sliding duration of 400 cycles in order to precisely verify this correlation. The first test at imposed displacement $\delta_i = \pm 40$ µm (uncertainty $\Delta\delta_i = 1$ µm) and a second test at imposed actuator force $F_{ai} = \pm 15$ N (uncertainty $\Delta F_{ai} = 0.5$ N).

The fretting loops seem to have similar patterns (Fig. 12). More precisely, friction tangential force is not constant during the sliding phases and a peak appears when displacement changes in direction as expected with ductile materials. It is noted that friction forces at imposed displacement are slightly higher and regular than those obtained at imposed actuator force (2.3 N

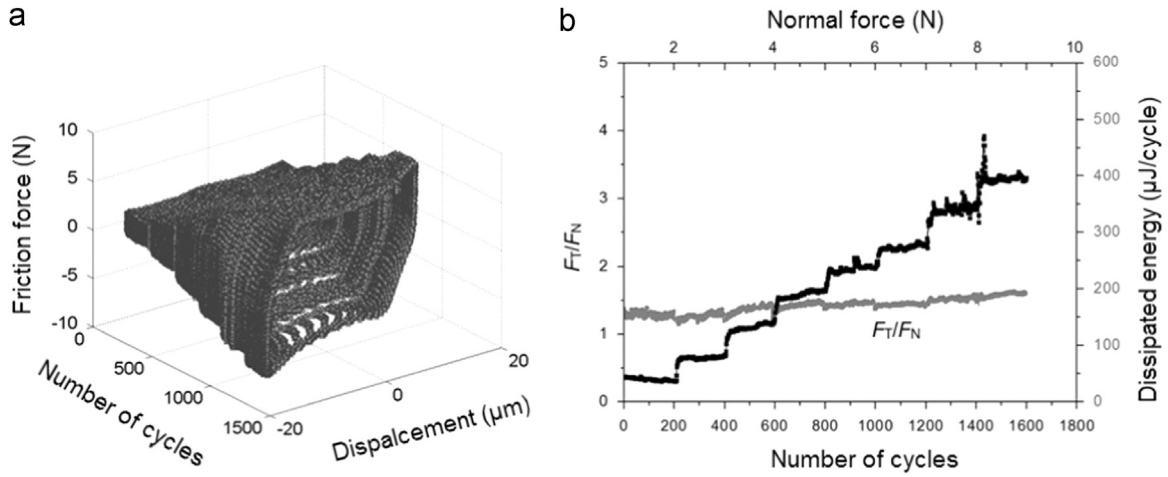

Fig. 10. Fretting tests by ramping normal force ($1 \leq F_N \leq 8$ N) at imposed displacement ($\delta_i \pm 15$ μm): (a) 3D cumulative log, (b) friction coefficient and dissipated energy change.

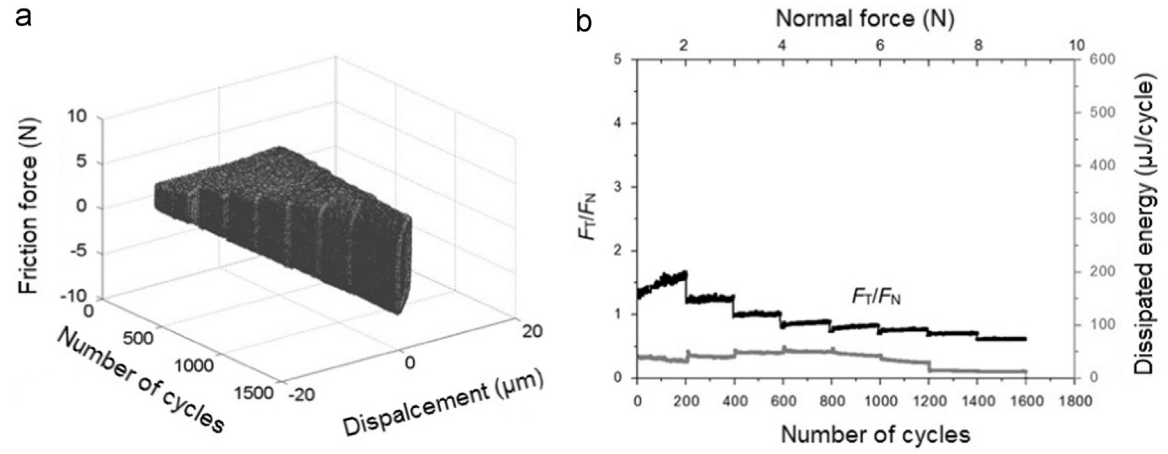

Fig. 11. Fretting tests by ramping normal force ($1 \leq F_N \leq 8$ N) at imposed actuator force ($F_{ai} \pm 6$ N): (a) 3D cumulative log, (b) friction coefficient and dissipated energy change.

compared to 2.2 N): the contact adapts its behavior through the friction force. Similarly, the recorded displacement amplitudes at imposed actuator force are lower than expected (± 38 μm instead of ± 40 μm): the contact accommodates its behavior by reducing its sliding amplitude.

More precisely, the response of the friction force during the sliding phases shows a better stability at imposed displacement and confirms that the control mode slightly affects surface interactions in the contact zone (Fig. 12). The analysis of time signals of force sensor by Fast Fourier Transform spectra (Fig. 13) only reveals the expected peak at 10 Hz with two significant harmonics at 30 and 50 Hz. Moreover no vibratory phenomenon associated with the resonance frequency of arm (90 100 Hz) is observed.

4.3.1. Role of excitation frequency

As excitation frequency could generate disturbances on the time signals of friction force, a series of tests at imposed displacement ($\delta_i = \pm 15$ μm) were performed with CuSn6/CuSn6 pairs in dry conditions at a normal load $F_N = 1$ N for frequencies ranged from 5 to 30 Hz. Time evolution of displacement shows a well defined sinusoidal shape for the full range of studied frequencies while friction force signals undergo more and more disturbances up to 30 Hz (Fig. 14). These considerations support the fact that accommodation mechanisms evolve with excitation frequency.

4.3.2. Role of applied load

As shown above, an imposed actuator force $F_{ai} = \pm 15$ N under a normal load $F_N = 1$ N approximately generates a relative displacement $\delta = \pm 40$ μm. Under higher normal forces, the actuator force needs to be higher to maintain an identical relative displacement. Therefore a test at imposed displacement $\delta_i = \pm 40$ μm under a normal load $F_N = 3$ N was compared to a test at imposed actuator force $F_{ai} = \pm 19$ N.

For similar amplitudes of displacement, imposed force test leads to lower mean friction coefficients (calculated from mean tangential friction force) and to lower cumulated dissipated energies (sum of all the successive loop areas during the test duration). Results for tests at 1 N and 3 N are gathered Table 1.

At a low normal load ($F_N = 1$ N), friction coefficients and dissipated energies remain close for the two control modes (gap lower than 10%) and there evolutions are rather stable. Under higher load ($F_N = 3$ N), friction coefficients and dissipated energies show more significant differences. Friction coefficients and cumulative dissipated energy are markedly higher at imposed displacement (gap around 27%).

As seen above with incremental loading tests, the friction coefficient is more stable when the displacement is the controlling parameter. In contrast, for imposed actuator force tests, dissipated energy does not remain constant with load increase because here, imposed forces are different. Differences in dissipated energy

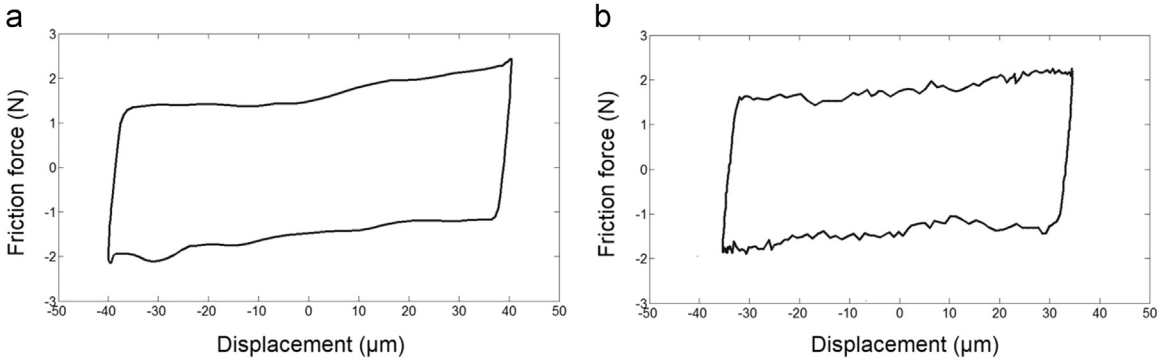

Fig. 12. Fretting loop (a) at imposed displacement δ_i ± 40 μm, (b) at imposed actuator force F_{ai} ± 15 N, (F_N 1 N, f 10 Hz).

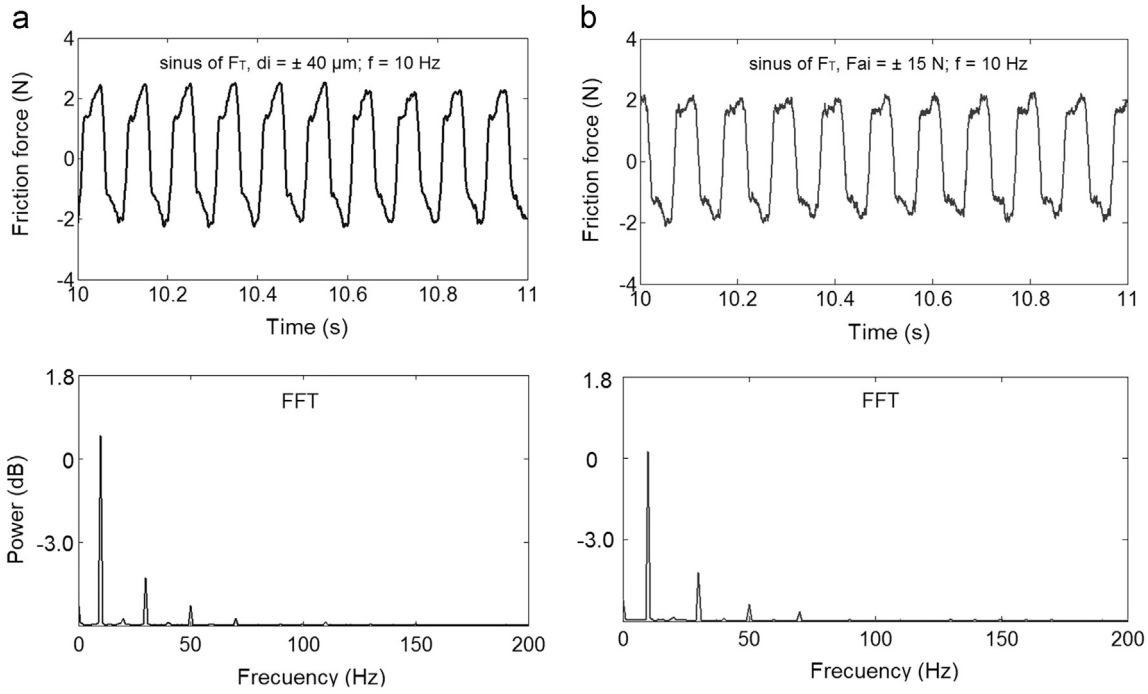

Fig. 13. Comparison of the temporal friction force and its associated Fast Fourier Transform spectra during 1 s from the cycle number 100 (a) at imposed displacement (δ_i ± 40 μm) and (b) at imposed actuator force (F_{ai} ± 15 N) (F_N 1 N, f 10 Hz).

between the two control modes are essentially linked to the fric tion force level. A contact working at imposed actuator force has the possibility to reduce its amplitude of displacement when the normal load increases. Such adjustments could imply modifica tions in the friction force. At imposed displacement, the friction force directly allows the contact accommodation.

At lower load, the evolution of dissipated energy as a function of the sliding distance instead of the number of cycles reveals a similar behavior for the two control modes. At higher load, con sideration between number of cycles and sliding distance could not explain any further the gap of dissipated energy (Fig. 15). This indicates that a modified accommodation mechanism occurs between these two tests.

4.3.3. Wear tracks observations

SEM observations show wear tracks slightly smaller for imposed force tests, consistent with the measured amplitudes of displacement (Fig. 16). Excavated and highly plastic deformed areas are observed in the central zone of the slider wear track and the facing sample, probably removed when opening the contact. At the edges of the contact, namely where the direction change occurs, the deformed material reveals superposed layers and more or less agglomerated debris. Debris of about 2 μm in diameter or length produced by fragmentation and grinding, scattered outside of the contact (Fig. 17).

Topographic profiles confirm the hollow shape of the wear tracks with lower volumes of matter in the form of ridges at track ends (Fig. 18). The counteracting samples show a reversed (com plementary) image of the topographic profiles with positive volume (matter excess) in the track center and a negative volume (removed matter) at track ends. Such W wear profiles, common to the two control modes, were described as an interlocking effect [11].

According to Fouvry et al. [12], this typical geometry results from a change in the stress distribution as a consequence of the modification of the surface geometry by the third body constituted by particle detachment from the surfaces. Indeed, at the beginning of the test, maximal contact pressure and shear stresses are con centrated in the central zone of the contact and favor the third body appearance (source flow). Later, a part of the third body (internal flow) piles up at the periphery of the wear track and

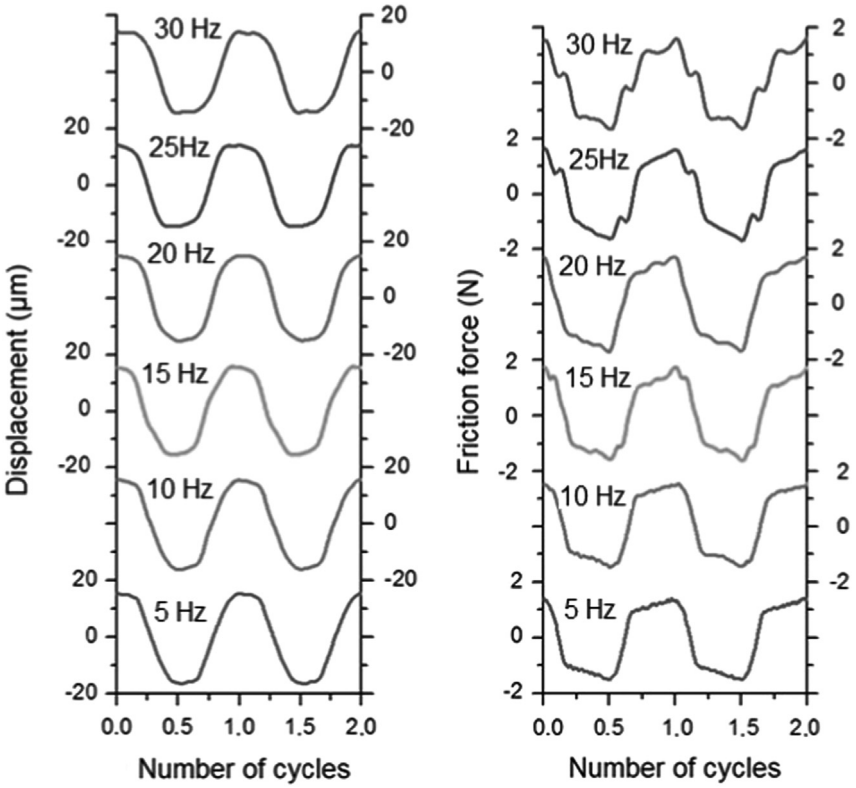

Fig. 14. Influence of excitation frequency at imposed displacement (δ_i ± 15 µm): (a) displacement (b) friction force (F_N 1 N).

Table 1
Mean values of friction coefficient and cumulative dissipated energy considers the control mode as a function of the applied load at imposed displacement (δ_i ± 40 µm) and at imposed actuator force (F_{ai} ± 15 N for F_N 1 N and ± 19 N for F_N 3 N) for CuSn6–CuSn6 pair (f 10 Hz, N_c 400 cycles).

Control mode	***Normal load***	1 N	3 N
Imposed displacement	Coefficient of fiction	1.59 ± 0.06	1.54 ± 0.03
	Dissipated energy (µJ)	241 ± 9 µJ	693 ± 36 µJ
Imposed actuator force	Coefficient of fiction	1.59 ± 0.05	1.22 ± 0.08
	Dissipated energy (µJ)	215 ± 6 µJ	503 ± 15 µJ

modifies the distribution of the contact pressure by increasing significantly stresses at the ends of the track.

4.3.4. Acoustic emission analysis

Figs. 19 and 20 compare the fretting loops built from acoustic emission (AE) hits in imposed displacement ($\delta_i = \pm 40$ µm) and in imposed actuator force ($F_{ai} = \pm 15$ N), synchronized with dis placement and tangential friction force signals. During the first 100 cycles, AE activity is mainly registered during the sliding phases. More precisely, at imposed actuator force, no AE activity occurs during the changes of sliding direction. During the fol lowing cycles, AE activity is observed during all cycle phases for the two control modes. Moreover, the location of the highest AE amplitudes migrates from the sliding phases at the beginning of the test to the loop extremities later.

This difference of acoustic activity at the loop extremities according to the control mode is consistent with a material plowing at every change in direction. This phenomenon is more pronounced at imposed displacement whereas the slider must come back exactly to the same position of the previous cycle, pushing debris out of the wear track. It is not the case at imposed actuator force because the displacement amplitude may be reduced during the test. In addition, most hits appearing at the loop extremities could be associated to the deformation and the pull out of debris from the wear track, in accordance with microscopic observations. The mean acoustic amplitudes for the two control modes are of the same order of magnitude: 30.8 ± 2.7 dB at imposed displacement and 31.5 ± 3.3 dB at imposed force. Nevertheless, the cumulative number of hits is higher at imposed displacement than at imposed force (Fig. 21).

The centroid frequency provides information on the type of failure mechanism that occurs inside the contact (Fig. 21). In our case, the frequency peaks are situated at 413 ± 22 Hz at imposed displacement and at 405 ± 32 Hz at imposed force. Such fre quencies are present during the overall test duration, which implies a common and stable mechanism for the two control modes where plastic deformation is clearly significant. These results are consistent with the studies of Baranov et al. [13] that concluded that sliding contacts subjected to plastic deformation could generate centroid frequencies close to 500 Hz.

4.3.5. Electrical contact resistance

A series of tests were carried out to study the changes of electrical contact resistance R_c under an applied normal load of $F_N = 6$ N for a duration of 25,000 cycles using the two control modes driven for achieving equivalent displacement amplitudes.

For displacement amplitude of $\delta_i = \pm 15$ µm, the electrical contact resistance as a function of time shows two distinct phases (Fig. 22a):

- The first phase matches with an established electrical contact, associated to a very low contact resistance ensuring the appropriate crossing for the electrical courant injected by the four wire circuit. The contact resistance remains constant at $R_c = 1.7$ mΩ at the first 1185 s (that is a total sliding distance of 0.55 m) at imposed displacement and during the first 863 s (sliding distance of 0.49 m) at imposed force.

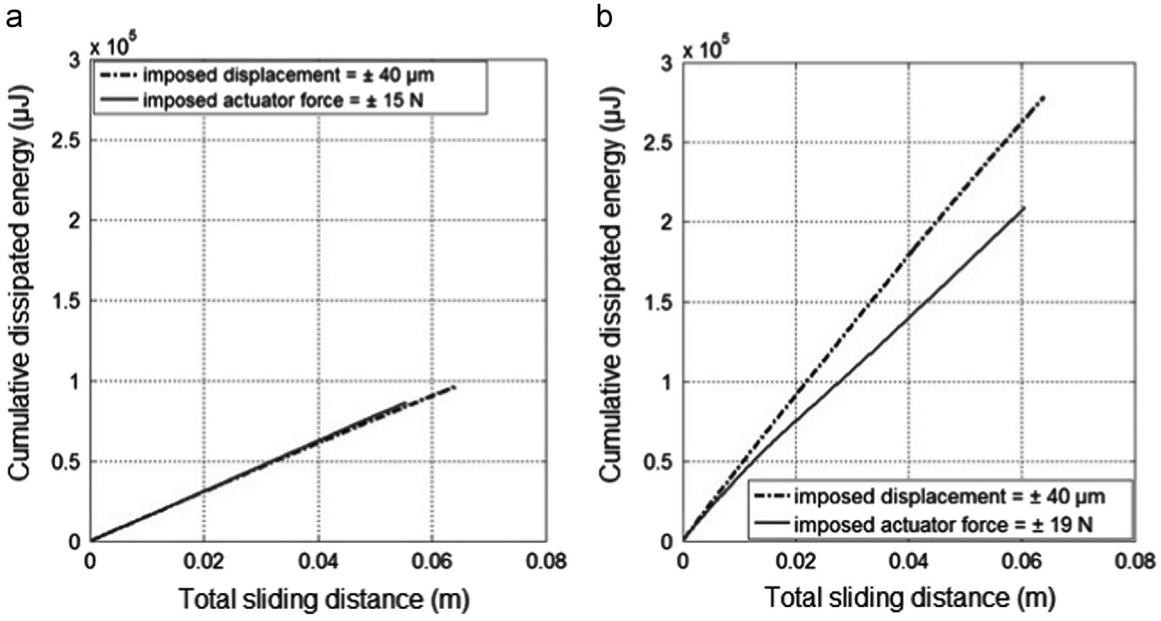

Fig. 15. Cumulative dissipated energy as a function of the total sliding distance at imposed, (a) (δ_i ± 40 µm) and at (F_{ai} ± 15 N) for F_N 1 N (b) (δ_i ± 40 µm) and (F_{ai} ± 19 N) for F_N 3 N with, f 10 Hz, N_c 400 cycles.

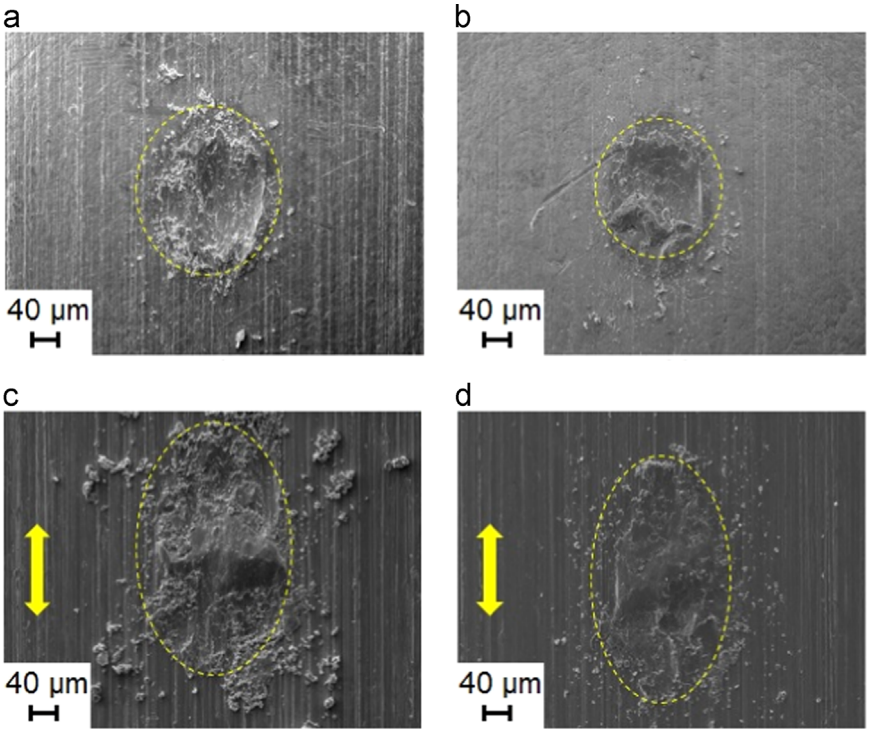

Fig. 16. Wear track observations by SEM: (a) CuSn6 hemispherical slider and (b) CuSn6 flat sample for imposed displacement tests at δ_i ± 40 µm; (c) CuSn6 hemispherical slider and (d) CuSn6 flat sample for imposed actuator force test (F_{ai} ± 15 N), with F_N 1 N, f 10 Hz, N_c 400 cycles.

- The second phase accounts for the conductivity loss in the contact. The electrical resistance starts increasing in an irre versible way to reach a maximal threshold of 10 Ω. The elec trical contact is damaged and the electrical resistance registers an instable behavior with small random drops during the test.

This similar behavior for the two control modes (Figs. 22a and 22c) is in accordance with the delayed formation of an insulating oxide layer, stable and sustainable inside the contact. Therefore, this insulating oxide layer is constituted later (1185 s instead of 863 s) the transition between the conductivity and the resistivity phases are longest at imposed displacement.

For a displacement amplitude of $\delta_i = \pm 40$ µm, the electrical contact resistance as a function of time shows a different behavior characterized by successive phases at low and high resistance (Fig. 22b):

- A first phase with a well established contact is found again during the first cycles with a stable and low value of $R_c = 0.17$ mΩ. This phase is shorter than at $\delta_i = \pm 15$ µm and as

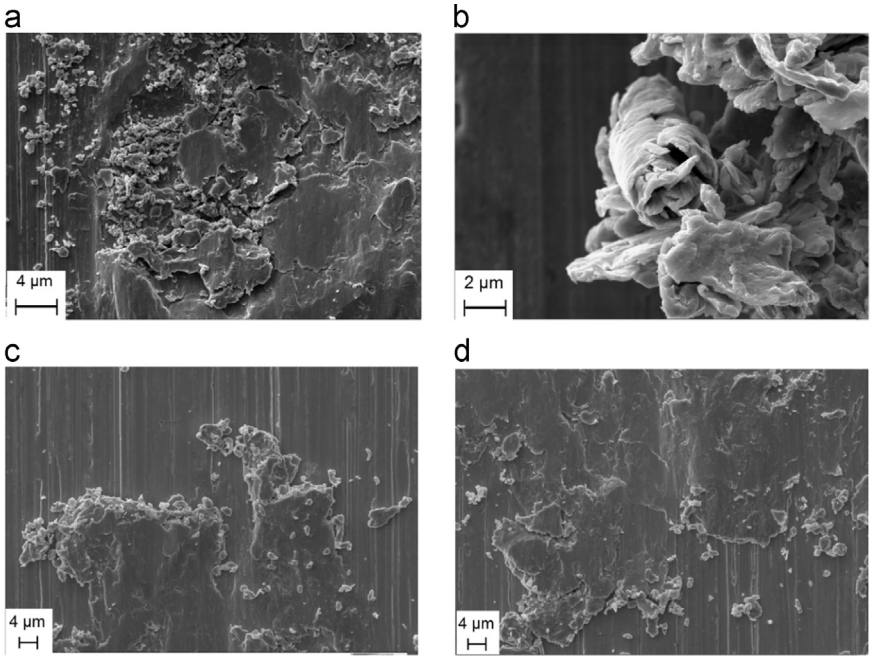

Fig. 17. Details of wear track observations by SEM: (a) center of the track and (b) track extremity of CuSn6 flat sample for imposed displacement tests at δ_i ± 40 µm; (c, d) track extremities of CuSn6 flat sample for imposed actuator force test (F_{ai} ± 15 N), with F_N 1 N, f 10 Hz, N_c 400 cycles.

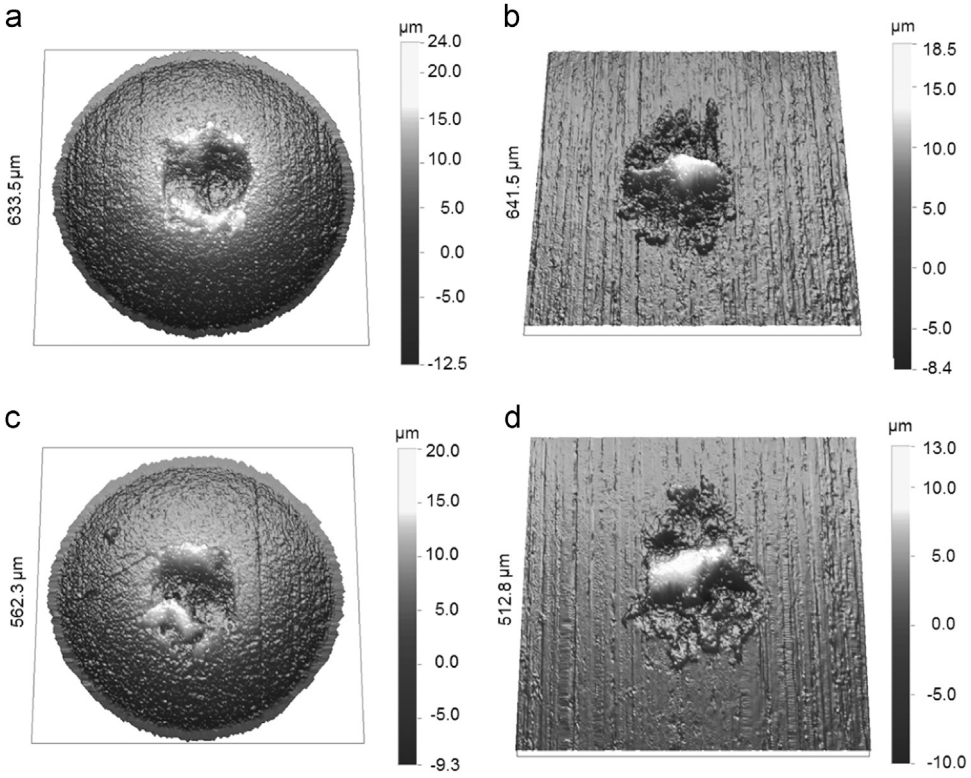

Fig. 18. Topographic images by optical profilometer: (a,b) imposed displacement test (δ_i ± 40 µm); (c,d) imposed actuator force test (F_{ai} ± 15 N), with F_N 1 N, f 10 Hz, N_c 400 cycles.

previously, extends a little bit at an imposed displacement (646 s) rather than at imposed force (561 s).

- A second phase deals with the sudden occurrence of higher resistance peaks relevant to a conductibility loss, followed by a more or less periodical recovery of low electrical contact resis tance. These peaks never exceed 4 Ω at imposed displacement while they reach up to 3 Ω at imposed force.

This electrical behavior change, similar for the two control modes (Figs. 22b and 22d), could be explained by considering that a sliding amplitude of ± 40 µm improve the circulation and ejec tion of debris, disturbing the oxide film stability between the surfaces and reduces the conductibility loss. The comparison of two modes shows that the duration of partial conductivity phases are more important at imposed displacement. In fact this reveals

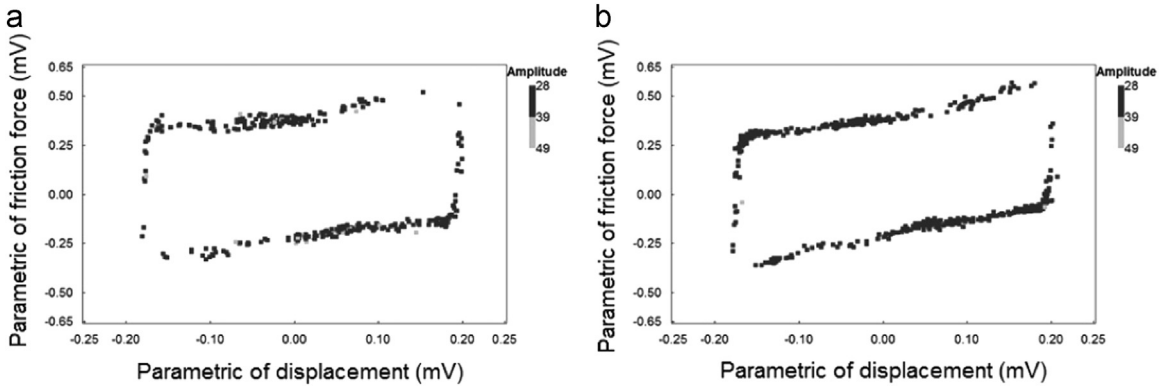

Fig. 19. Amplitude of acoustic emission hits along the fretting loops at imposed displacement (δ_i ± 40 μm), F_N 1 N, f 10 Hz (a) during the first 100 cycles, (b) between 300 and 400 cycles.

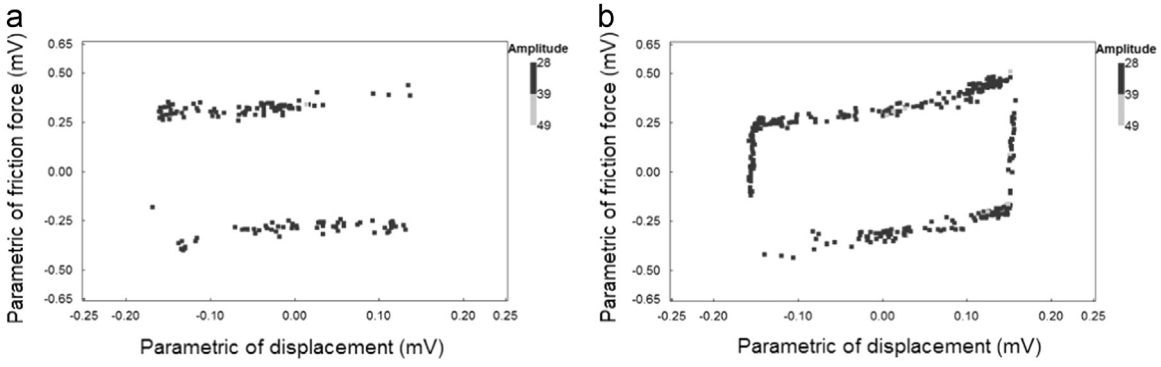

Fig. 20. Amplitude of acoustic emission hits along the fretting loops at imposed actuator force (F_{ai} ± 15 N), F_N 1 N, f 10 Hz (a) during the first 100 cycles, (b) between 300 and 400 cycles.

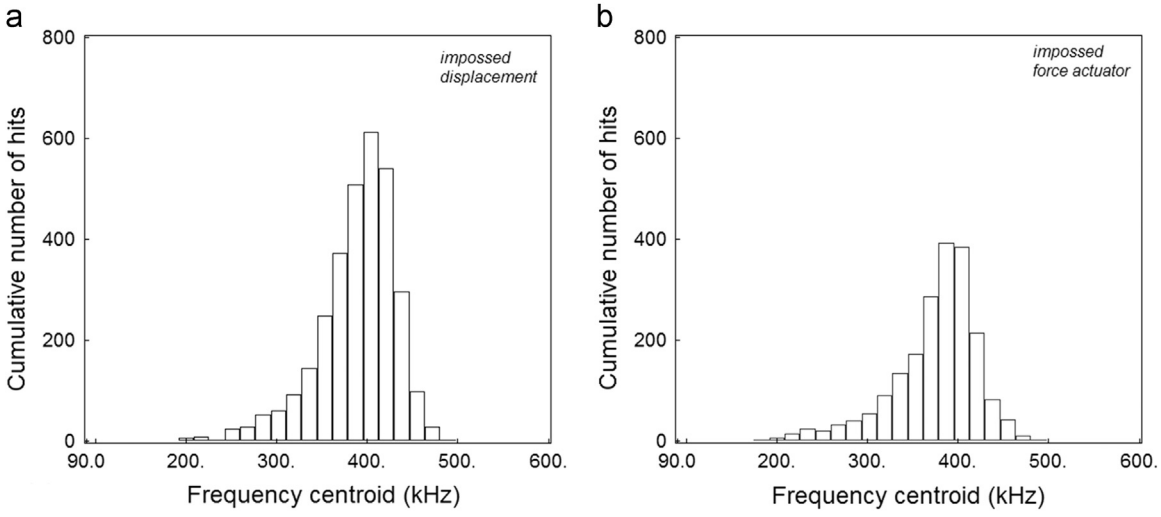

Fig. 21. Cumulative number of hits as a function of the centroid frequency (a) at imposed displacement (δ_i ± 40 μm), (b) at imposed force (F_{ai} ± 15 N), F_N 1 N, f 10 Hz.

that this control mode promote a higher wear's kinetic. However, the conductivity loss is an irreversible process in time.

5. Influence of the contacting materials

Tests under imposed displacement $\delta_i = \pm 40$ μm, at frequency $f = 10$ Hz and load $F_N = 1$ N were carried out with three pairs of materials: CuSn6/CuSn6 (metal/metal), CuSn6/Al_2O_3 (metal/ceramic) and CuSn6/PTFE (metal/polymer).

For metal/metal pairs, the tangential force increases along the sliding phase and the presence of tips is observed at the end of each sliding phase (Fig. 23a). The average coefficient of friction and the dissipated energy are high. This behavior is usually associated to strong interactions that occur between ductile metals (plastic deformation in the contact with asperity interlocking and strong adhesion).

For metal/ceramic pairs, the loops are almost rectangular where tangential forces are constant and without tips at the ends (Fig. 23b). The friction coefficient remains constant but the dissipated energy is

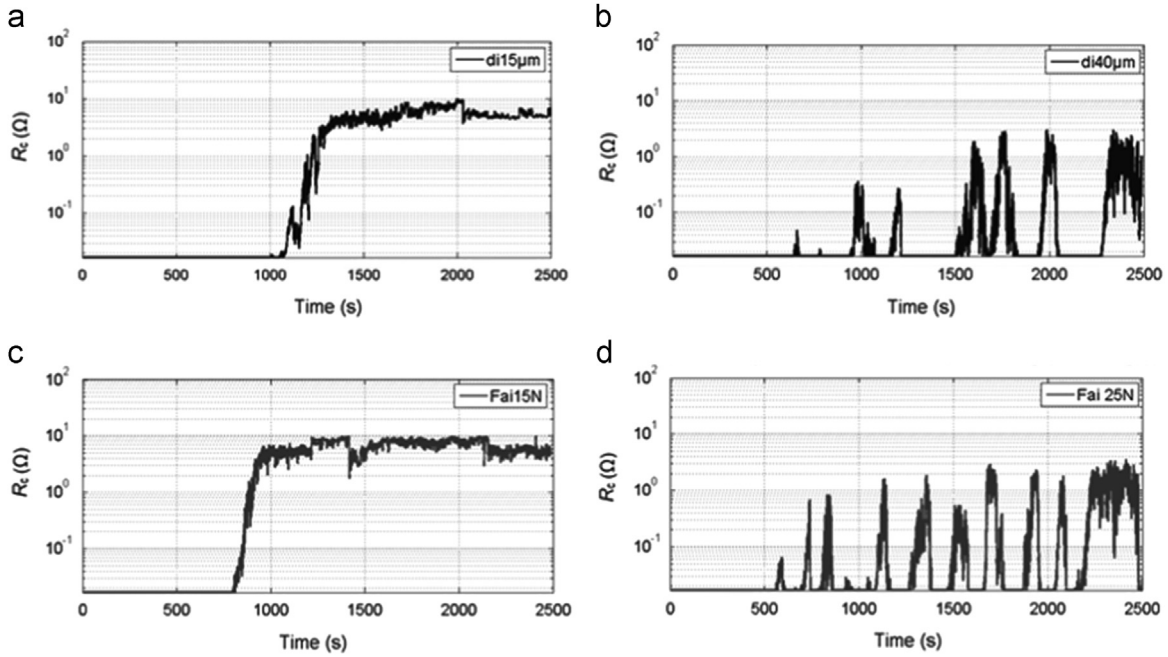

Fig. 22. Temporal evolution of the electrical resistance of a CuSn6–CuSn6 contact (a) at imposed displacement (δ_i ± 15 μm), (b) at imposed displacement (δ_i ± 40 μm), (c) at imposed force (F_{ai} ± 15 N), and (d) at imposed force (F_{ai} ± 25 N), I 100 mA, F_N 6 N, f 10 Hz N_c 25,000 cycles.

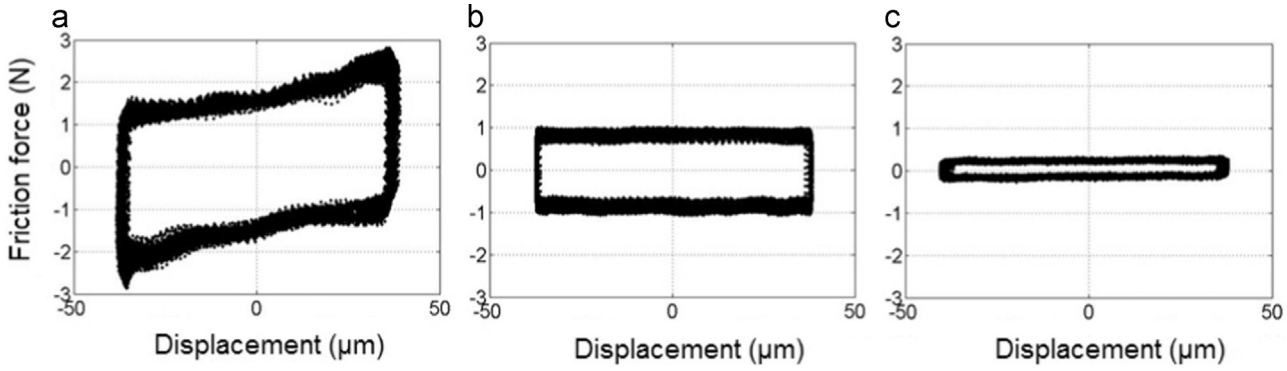

Fig. 23. Material influence on fretting loops: (a) CuSn6/CuSn6 pair; (b) CuSn6/Al_2O_3 pair; (c) CuSn6/PTFE pair.

still quite high. Adhesion is reduced but the ceramic hardness causes a significant abrasive contribution.

For metal/polymer pairs, the shape of the loops is similar to metal/ceramic pairs, but the level of the tangential force is greatly reduced and presents very little scattering, involving a low friction coefficient and low dissipated energy (Fig. 23c). This behavior illustrates the weak interactions (weak adhesion) in this pair of materials as a consequence of the low surface energy of PTFE.

Vibration measurements were performed on the three tested pairs (metal/metal, metal/ceramic and metal/polymer). Although the measured resonance frequency for the three couples remains unchanged, a proportional coupling is observed between the vibra tion intensity and the level of the tangential forces: the more tan gential friction forces, the higher intensity of the vibration signals. Thus, the nature of the rubbing materials is directly related to the vibration intensity transmitted to the system (arm of the device).

6. Conclusions

This study precisely characterizes the device behavior, that is to say, its “signature”, through the analysis of fretting loops. The influence of two motion generating modes (imposed displacement and imposed actuator force) on slip regimes, the effects resulting from artifacts due to sensors on the fretting loops, the role of compliance of the system (high stiffness devices result in significant dissipation of energy through the contact), the excitation frequency and the con tacting materials on the tribological response of the contact.

The two control modes involve different local accommodation mechanisms inside the contact zone. At imposed displacement, the contact is able to accommodate by varying the friction force while at imposed actuator force, the contact adjustment occurs by varying the displacement amplitude. Under a low normal load, the values of friction coefficients and dissipated energies are very similar, but differences increase with higher loads. Dissipated energy changes as a function of the sliding distance confirms this trend while significantly depending on friction coefficient (higher for imposed displacement compared to imposed actuator force). A vibratory analysis shows that the resonance frequencies are very sensitive to the excitation frequency, but the intensity of vibration is proportional to the tangential forces (coupling materials).

Observation of the wear tracks reveals plastic deformation mechanisms leading to conformal profiles between the two

contacting surfaces, with lower production of debris pulled out the contact. Acoustic signatures confirm the occurrence of a common failure mechanism with a centroid frequency close to 400 Hz for the two control modes. However, the distribution of hits along the fretting loops denotes different locations for interactions during the early stages according to the control mode. Hence, under imposed displacement the number of hits is higher, while the amplitude of hits is lower, than under imposed actuator force.

Electrical contact resistances show similar behaviors for the two control modes. The electrical contact damage gives rise to a higher increase in contact resistance from a sliding distance threshold. This threshold is as high as the displacement amplitude and excitation frequency are high.

The influence of the contact materials (ductile, hard and brittle, or poorly adhesive) shows that the deformation and adhesion of materials is directly related to the shape modifications of the fretting loops (increased friction force, presence of tips) and thus the dissipated energy levels. Material behavior also plays a fun damental role on the magnitude of the interactions with the sys tem (couplings observed from vibration measurements).

References

[1] M. Antler, Contact fretting of electronic connectors, IEICE Trans. Electron. E82-C (1) (1999) 3–12.

[2] V. Siddeswara Prasad, M. Prashant, J. Nagaraju, An experimental study to show the behaviour of electrical contact resistance and coefficient of friction at low current sliding electrical interfaces, in: Proceedings of Electrical Contacts (Holm), IEEE 57th Holm Conference, 2011, pp. 1–7.

[3] S. Noël, D. Alamarguy, A. Brézard-Oudota, P. Gendre, An investigation of fretting wear behaviour of nickel coatings for electrical contacts application in dry and lubricated conditions, Wear 301 (2013) 551–561.

[4] Y. Berthier, L. Vincent, M. Godet, Fretting fatigue and fretting wear, Tribol. Int. 22 (4) (1989) 235–242.

[5] A. Ramalho, J.-P. Celis, Fretting laboratory test: Analysis of the mechanical response of tests rigs, Tribol. Lett. 14 (3) (2003) 187–196.

[6] S. Fouvry, P. Kapsa, L. Vincent, Analysis of sliding behaviour for fretting loadings: determination of transition criteria, Wear 85 (1995) 35–36.

[7] K. Elleuch, S. Fouvry, Wear analysis of A357 aluminum alloy under fretting, Wear 253 (2002) 662–672.

[8] S.R. Pearson, P.H. Shipway, J.O. Abere, R.A.A. Hewitt, The effect of temperature on wear and friction of high strength steel in fretting, Wear 303 (2013) 622–631.

[9] J. Hintikka, A. Lehtovaara, A. Mäntylyä, Non-Coulomb friction in gross sliding fretting conditions with aluminum bronze against quenched and tempered steel, Tribol. Int. 79 (2014) 151–161.

[10] D.M. Mulvihill, M.E. Kartal, A.V. Olver, D. Nowell, D.A. Hills, Investigation of non-Coulomb friction behaviour in reciprocating sliding, Wear 271 (5) (2011) 802–816.

[11] M.R. Hirsch, R.W. Neu, A simple model for friction evolution in fretting, Wear 301 (1) (2013) 517–523.

[12] S. Fouvry, P. Kapsa, L. Vincent, Quantification of fretting damage, Wear 200 (1996) 186–205.

[13] V.M. Baranov, E.M. Kudryavtsev, G.A. Sarychev, V.M. Schavelin, Acoustic emission in friction, 53, Elsevier, The Netherlands, 2011.